



Wire and arc additive manufacturing of Fe-based shape memory alloys: Microstructure, mechanical and functional behavior

Igor O. Felice^{a,*}, Jiajia Shen^{a,b}, André F.C. Barragan^b, Isaque A.B. Moura^{a,b}, Binqiang Li^{c,d}, Binbin Wang^d, Hesamodin Khodaverdi^e, Maryam Mohri^f, Norbert Schell^g, Elyas Ghafoori^{f,h}, Telmo G. Santos^{a,i}, J.P. Oliveira^{a,b,*}

^a UNIDEMI, Department of Mechanical and Industrial Engineering, NOVA School of Science and Technology, Universidade NOVA de Lisboa, Caparica 2829-516, Portugal

^b CENIMAT/I3N, Department of Materials Science, NOVA School of Science and Technology, Universidade NOVA de Lisboa, Caparica 2829-516, Portugal

^c Western Superconducting Technologies Co., Ltd., Shaanxi Province Engineering Laboratory for Aerial Material, Xi'an 710018, China

^d National Key Laboratory for Precision Hot Processing of Metals, School of Materials Science and Engineering, Harbin Institute of Technology, Harbin 150001, China

^e School of Metallurgy and Materials Engineering, College of Engineering, University of Tehran, Tehran, Iran

^f Empa, Swiss Federal Laboratories for Materials Science and Technology, Dübendorf 8600, Switzerland

^g Helmholtz-Zentrum Hereon, Institute of Materials Physics, Max-Planck-Str. 1, Geesthacht 21502, Germany

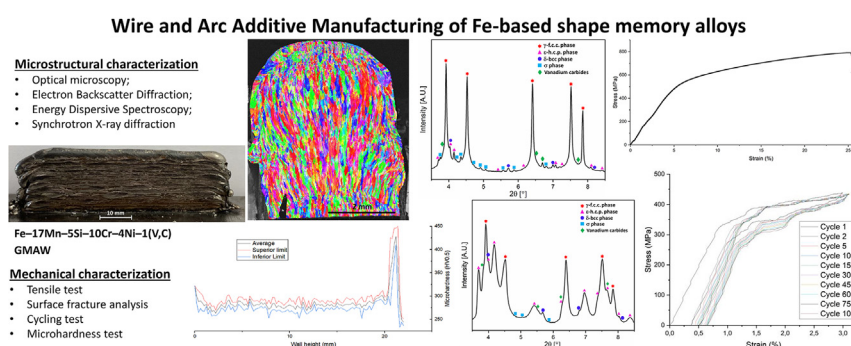
^h Institute for Steel Construction, Faculty of Civil Engineering and Geodetic Science, Leibniz University Hannover, Hannover 30167, Germany

ⁱ Laboratório Associado de Sistemas Inteligentes, LASI, 4800-058 Guimarães, Portugal

HIGHLIGHTS

- A novel iron-based shape memory alloy was successfully deposited by wire and arc additive manufacturing.
- As-deposited material was predominantly composed by FCC γ phase with a columnar dendritic morphology.
- High mechanical performance was observed for yield strength, fracture stress, elongation, cyclic repetitibility and hardness.
- Uniaxial loading induced the FCC $\gamma \rightarrow$ HCP ϵ phase transformation and resulted in a ductile fracture.

GRAPHICAL ABSTRACT



ARTICLE INFO

Article history:

Received 28 February 2023

Revised 27 April 2023

Accepted 13 May 2023

Available online 18 May 2023

Keywords:

Shape memory alloys
Iron-based
Additive manufacturing
Arc-based DED
Phase transformation
Characterization

ABSTRACT

Shape memory alloys (SMA) are a class of smart materials with inherent shape memory and superelastic characteristics. Unlike other SMAs, iron-based SMAs (Fe-SMA) offer cost-effectiveness, weldability, and robust mechanical strength for the construction industry. Thus, applying these promising materials to advanced manufacturing processes is of considerable industrial and academic relevance. This study aims to present a pioneer application of a Fe-Mn-Si-Cr-Ni-V-C SMA to arc-based directed energy deposition additive manufacturing, namely wire and arc additive manufacturing (WAAM), examining the microstructure evolution and mechanical/functional response. The WAAM-fabricated Fe-SMAs presented negligible porosity and high deposition efficiency. Microstructure characterization encompassing electron microscopy and high energy synchrotron X-ray diffraction revealed that the as-deposited material is primarily composed by γ FCC phase with modest amounts of VC, ϵ and σ phases. Tensile and cyclic testing highlighted the Fe-SMA's excellent mechanical and functional response. Tensile testing revealed a yield strength and fracture stress of 472 and 821 MPa, respectively, with a fracture strain of 26%. After uniaxial tensile loading to fracture, the $\gamma \rightarrow \epsilon$ phase transformation was clearly evidenced with post-

* Corresponding authors at: CENIMAT/I3N, Department of Materials Science, NOVA School of Science and Technology, Universidade NOVA de Lisboa, Caparica 2829-516, Portugal

E-mail addresses: i.felice@campus.fct.unl.pt (I.O. Felice), jp.oliveira@fct.unl.pt (J.P. Oliveira).

mortem synchrotron X-ray diffraction analysis. The cyclic stability during 100 load/unloading cycles was also evaluated, showcasing the potential applicability of the fabricated material for structural applications.

© 2023 The Authors. Published by Elsevier Ltd. This is an open access article under the CC BY license (<http://creativecommons.org/licenses/by/4.0/>).

1. Introduction

Shape memory alloys (SMAs) are a class of advanced and smart materials that can recover their original shape even after a non-elastic external strain is imposed. This recovery occurs due to a reversible phase transformation between a low temperature martensitic phase and high temperature austenite. When an external strain is imposed at a lower temperature in the martensitic phase, recovery of the apparently permanent deformation occurs due to the so-called shape memory effect (SME) upon heating up to the austenitic domain. Likewise, if sample deformation occurs in the high temperature regime, i.e., within the austenitic phase field, superelasticity (SE) is the governing phenomena [1–3]. SMAs' valuable functional characteristics and suitable mechanical properties make them suitable in various fields including civil, aerospace, medical, and automotive industries [4,5].

Among the various SMA materials, NiTi is the most widely researched and utilized due to its functional properties, high strength, ductility, and biocompatibility [6]. NiTi has important applications in energy dissipation structures [7], such as passive dampers [8], cross-bracing cables [9], and seismic isolators [10]. However, its high cost compared to other alloys hinders its usage in some sectors, especially for those with lower value-added. Otherwise, iron-based shape memory alloys (Fe-SMAs) have been extensively investigated for structural applications since the discovery of their SME in 1982 [11]. Advantages such as the low cost of raw materials, corrosion resistance, stable recovery stresses, suitability to manufacturing process (weldability and machinability, for example), and good resulting mechanical and functional properties (namely mechanical strength, elastic stiffness, and recovery stresses), increase their attractiveness and applicability in various fields [11–19].

The SME of Fe-SMAs relies on a thermodynamically reversible phase transformation between γ FCC austenite, the high temperature phase, and HCP ε martensite, the low temperature phase [10]. Fe-SMAs can be constrained during this phase transformation to induce prestress, which strengthens the material. This principle of Fe-SMAs strengthening is illustrated in Fig. 1. Some prominent applications of these Fe-based materials rely on mechanical and hydraulic line couplings (including larger pipe diameters), prestressing tendons and beams, crane rail joint bars, rubber bearings,

friction pendulum systems and bridge girders as structurally-oriented components [20]. Fe-SMAs were previously thought to have negligible superelasticity (SE) despite good energy dissipation and low-cycle fatigue performance [21]. However, recent studies have shown that SE can be increased through thermo-mechanical treatments and microstructure modification [1,22]. In general, SE for these materials relies on the non-thermoelastic martensitic transformation between γ and ε phases [23].

Recently, an innovative Fe-SMA composition of Fe-17Mn-5Si-10Cr-4Ni-1(V,C) has been developed and optimized to increase the performance of prestressed strengthened structures. Some studies demonstrated the formations of elastic strain fields near the vanadium carbide (VC) precipitates, improving both SME and SE [1]. Also, these precipitates can provide preferential nucleation sites for the ε phase and a high density of stacking faults in the γ matrix. Furthermore, it has also been shown that special textures of this material can improve its SE response [16,19,25–27]. The abovementioned special textures that can be obtained by appropriate thermomechanical processing that favor the improvement of the superplastic response of the Fe-based SMAs imply that the need to understand how the solidification microstructure in additively manufactured Fe-SMAs impact the functional and mechanical performance and if thermomechanical processing is needed after the material deposition.

Established the benefits and potentialities of Fe-SMAs, selecting the optimal manufacturing process is critical to achieve the desired design characteristics, particularly in terms of geometric design and strength. Conventional manufacturing methods, such as casting, forging, and milling, impose significant limitations and difficulties in creating complex-shaped components based on SMAs, thereby constraining the application of these smart materials [4]. Consequently, additive manufacturing (AM) has become a promising alternative for producing SMA-based components.

The fabrication industry has witnessed significant innovation with the advent of AM technologies, which employ a layer-by-layer deposition process to create near-net-shape 3D parts, thereby reducing material losses and production time. [28]. AM encompasses a range of categories that are characterized according to the type of energy source and material feedstock used. In the case of metal components, the commonly employed technologies are powder bed fusion (PBF) and directed energy deposition (DED).

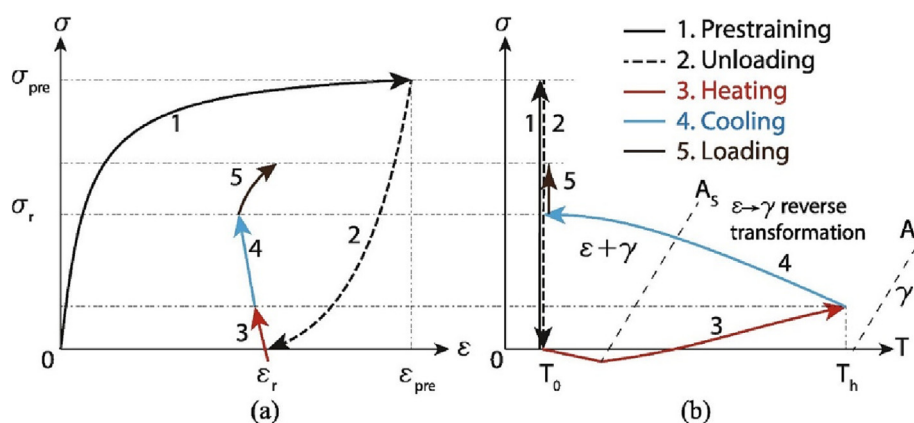


Fig. 1. Strengthening principle of Fe-SMAs. (a) Stress-strain behavior. (b) Stress-temperature behavior [24].

PBF selectively melts or sinters a metallic powder bed using a high-energy power source, such as a laser or electron beam, based on the desired design. On the other hand, DED involves creating a melt pool using a heat source, like laser, electron beam, or plasma arc, and adding filler materials in the form of powder or wire into the melt pool. [29,30]. Despite being a recent development, several components have already been fabricated through additive manufacturing, mainly in the aerospace, naval, automotive, healthcare and oil + gas industries [31]. Therefore, AM has enormous potential to be deployed in manufacturing SMA parts due to the significant limitations of conventional subtractive methods, including high tool wear and inability to build complex parts. Additionally, the deposition parameters significantly affect the microstructure of the final component and its associated thermomechanical behavior, which may require post-processing steps such as heat treatments or machining to optimize the final product [32].

Currently, some AM technologies, particularly laser and electron beam-based, are in a progressive usage path for SMAs [28–30]. LPBF, specifically, has been used to produce Fe-SMA parts. Thus, Shahverdi et al. [33] observed a superior SE and SME in LPBF Fe-SMA when compared to the same alloy manufactured by conventional methods. Also, Kim et al. [34] compared this metallic alloy with shape memory polymers. Ferreto et al. [35] applied for the first time the iron-based Fe–17Mn–5Si–10Cr–4Ni shape memory alloy to the LPBF process and Yang et al. [36] studied the effect of the Fe-SMA volumetric energy density on the densification, microstructures, tensile mechanical properties, and shape memory performance of parts manufactured by LPBF. Despite the great academic and industrial relevance, good precision and accuracy, laser and electron beam-based AM technologies are associated with high equipment costs, lower deposition rates and limitations in producing large components compared to arc-based DED AM technologies. Wire and Arc Additive Manufacturing – WAAM, which is based on the technologies Gas Metal Arc Welding (GMAW), Plasma Arc Welding (PAW) or Gas Tungsten Arc Welding (GTAW), employs a heat source to achieve high deposition rates and is a recognized manufacturing alternative with great academic and industrial relevance [37].

Currently, the majority of literature focuses on the advancement and analysis of arc-based DED AM in NiTi SMAs. [37–39]. Although NiTi is the most used SMA, there is potential for further exploration of Cu- and Fe-based SMAs. Therefore, based on the literature review, it is important to, not only investigate the use of AM for Fe-SMAs, but also explore a wider range of AM processes that can be utilized for these smart alloys.

In this sense, it has not yet been reported in the literature the application of arc-based AM processes for manufacturing high performance Fe-based SMA components, and herein lies the key scientific problem in this research: assessing the feasibility of the process for these alloys and evaluating the mechanical and microstructural characteristics of the resultant material, thereby launching further investigations. The successful production of Fe-based SMA utilizing GMAW-based WAAM is reported for the first time in this work. The microstructure and mechanical properties were evaluated based on electron microscopy, synchrotron X-ray diffraction, hardness, and mechanical testing, being posteriorly correlated to the thermal cycle experienced by the material during deposition. The findings of this study have the potential to boost future works and enable a wider implementation of WAAM technology in the manufacturing of SMAs.

2. Materials and methods

2.1 Materials and experimental procedure

The Fe-SMA utilized in this study has a chemical composition of Fe-17Mn-5Si-10Cr-4Ni-1(V, C) (wt. %). A single wall was fabricated

using a DED – Arc + wire welding torch attached to a 3-axes moving head within a working volume of $2.7 \times 1.9 \times 2.0$ m. A PRO MIG 3200 conventional power source from KEMPY was utilized to deposit a 1 mm diameter wire of the aforementioned alloy onto a mild steel grinded substrate with a dimension of $150 \times 60 \times 8$ mm, using constant voltage settings. The length of the as-built wall was set to 60 mm, and a 2-minute dwell time was established to ensure that each deposition began only after the previously deposited layer had cooled to a temperature below 100°C , thereby preventing distortions and defects caused by high heat accumulation that are typical in Wire Arc Additive Manufacturing (WAAM) [40]. This also aimed to prevent cold cracking generation upon cooling and to obtain better wettability between layers [41,42]. A total of 18 layers were deposited vertically, and the optimized deposition parameters are detailed in Table 1. These parameters were defined after a sequence of deposition tests involving alloys of similar metallurgical behavior and composition owing to the limited availability of material. The final deposited wall is illustrated in Fig. 2.

Subsequently, the wall edges were symmetrically cut in a way that the remaining part consisted of a 45 mm length structure. To remove the intrinsic surface waviness caused by the WAAM stair-stepping effect [43], lateral milling was applied using an *Enrique Holke EHF1010*. The cutting parameters were carefully adjusted to the values listed in Table 2, and to maintain low operation temperatures (of both tools and material), a constant lubricant feed and manual airflow were applied. This step was crucial to preserve the as-deposited microstructural and mechanical characteristics of the as-built material for the subsequent analysis. A macroscopic geometrical evaluation of the cross-section was performed to estimate the wall surface, along with the calculation of the material's deposition efficiency. The efficiency (E_f) is defined as the ratio between the wall cross-section *useful area* – after milling (A_{usef}) – and the *deposited area* – before milling (A_{dep}). Area measurements were determined using license-free imaging software, and the cross-section profiles were virtually reconstructed using an in-house developed software. To calculate the waviness parameter (W), a midline of the virtually reconstructed profile was created to ensure that the sum of values above the line was numerically equal to the sum of values below it (refer to Fig. 3). The absolute values of the distances (d_i) between the profile points and the midline were calculated using Equation (1), where parameters A, B, and C represent the coefficients of the midline equation and x_i, y_i are the coordinates of the point on the profile. These distances were used to calculate the waviness parameter (W), through Equation (2) [44].

$$d_i = \frac{Ax_i + By_i + C}{\sqrt{A^2 + B^2}} \quad (1)$$

$$W = \frac{\sum_{i=1}^N |d_i|}{N} \quad (2)$$

The porosity level was estimated using the gravimetry technique, which is a simple and cost-effective method that provides reliable results when compared to other common methodologies,

Table 1
Detailed deposition parameters for manufacturing of Fe-based SMA.

| Welding mode | GMAW – continuous mode DC + |
|------------------------------|---------------------------------------|
| Wire feed speed | 3 m/min |
| Travel speed | 480 mm/min |
| Voltage | 18 V |
| Contact tip to work distance | 10 mm |
| Shielding gas | M21 – 82% Argon & 18% CO ₂ |
| Gas flow rate | 15 L/min |

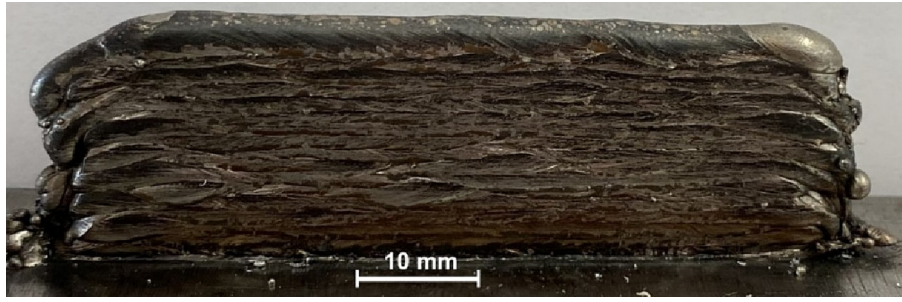


Fig. 2. As-built Fe-SMA wall after complete deposition.

Table 2
Cutting parameters for lateral milling process.

| | |
|---------------|-------------|
| Spindle speed | 260 rev/min |
| Cutting speed | 75 mm/min |
| Depth of cut | 0.4 mm |

such as microscopy or computed tomography [45]. For each of the three samples obtained along the as-built wall, mass measurements were acquired in air and when immersed in pure acetone. The wire feedstock material was used as reference. Density (ρ) was calculated using Eq. (3), where ρ_{liq} is the acetone density ($7.96 \times 10^5 \text{ kg/m}^3$), m_{air} is the mass measured in air and m_{liq} is the mass measured when immersed. The volume of voids percentage (VV) was calculated using Eq. (4) and enables a comparison between the samples' density and that of a reference (ρ_{ref} – feedstock material density in the case of this study).

$$\rho = \frac{\rho_{liq} \cdot m_{air}}{m_{air} - m_{liq}} \quad (3)$$

$$VV = \frac{(\rho_{ref} - \rho_{sample})}{\rho_{ref}} \quad (4)$$

2.2. Microstructural characterization

The wall cross-section was prepared for microstructure characterization by embedding, grinding, and polishing using 3 and 1 μm diamond paste. Macro and micrographs were taken after etching the cross-section of the wall using Keller's etching reagent for approximately 13 min. As a result of the chemical heterogeneity throughout the sample, preferential etching of the microstructure occurred. The material microstructure was using with a *Leica DMI5000M* inverted optical microscope (OM).

Electron Backscatter Diffraction (EBSD) was used to determine crystallographic orientation, grain measurements, and existing phases. The complete image dataset was analyzed with a threshold angle defined to 10° . The material's elemental composition was determined by Energy Dispersive Spectroscopy (EDS) along two 250 μm parallel lines located on the top region of the wall.

To further analyze the phase composition of the material in the as-deposited and after tensile testing, synchrotron X-ray diffraction (SXRD) was used at the P07 beamline of the High Energy Materials Science (HEMS), PETRA III/DESY, using a wavelength of 0.1423 Å and an incident beam of $0.2 \times 0.2 \text{ mm}$. A Perkin-Elmer detector was used to acquire the 2D Debye-Scherrer diffraction rings images and provided qualitative information on the grain size and texture of the analyzed material. LaB_6 powder was used for calibration. The raw data was processed using in-house developed python routines.

2.3. Mechanical characterization

Sub-sized specimens for mechanical testing were extracted from the waviness-free wall surface using electro-discharge machining (EDM) parallel to the deposition direction. The geometry was designated based on previous approaches to test sub-sized specimens [46]. Due to the reduced dimensions obtained, 2 specimens were used for the tensile testing and 1 used for cycling tests at ambient temperature, utilizing a *Shimadzu AG-50kNG* universal tensile machine. The tests were performed with a constant displacement rate of 0.3 mm/min. The fracture surface was analyzed using a Scanning Electron Microscope (SEM) *SU3800 Hitachi*. To assess the functional fatigue of the as-deposited material, mechanical cycling was carried out. The testing procedure involved straining the material to 3% followed by unloading to a zero-stress condition. This was repeated for a total of 100 cycles. From the load/unload testing, the evolution of irrecoverable strain, absorbed energy and maximum stress with the number of cycles was determined. The residual strain observed at the test zero stress point characterized the irrecoverable strain for each cycle. The absorbed energy was determined by calculating the difference between the energy expended during loading and that recovered during unloading. Both expended and recovered energy was computed by integrating the stress-strain curve using data from the test.

In one of the cross-sections of as-built wall, a microhardness map was constructed using a *Mitutoyo HM-112 Micro-Vickers Hardness Testing Machine*, with a load of 0.5 kgf ($\text{HV}_{0.5}$) applied for 10 s. A vertical distance of 200 μm between 2 consecutive indentations was used to avoid any interference between consecutive measurements [47].

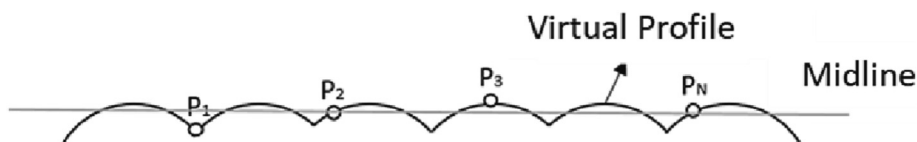


Fig. 3. Schematic illustration of the reconstructed virtual profile and the midline to determine surface waviness.

3. Results and discussion

The surface waviness (W) of the as-built wall was evaluated by analyzing the cross section. The measurements were restricted to the useful area of the deposited material and the final layers were excluded due to the top concavity. The lateral surface waviness was found to be $104\text{ }\mu\text{m}$ and $125\text{ }\mu\text{m}$ for the two sides of the wall, respectively. This waviness difference was expected and can be related to an intrinsic process limitation associated to arc-based processes. The behavior of the molten pools becomes more compli-

cated when metal droplets are deposited on non-level surfaces. This is due to the unbalanced forces and non-horizontal surfaces. Consequently, undesirable fluid flow patterns and bead morphol-

Table 3

Density and volume of voids for the as-deposited Fe-SMA samples.

| Sample | Density (10^6 kg/m^3) | Volume of voids (%) |
|--------|----------------------------------|---------------------|
| 1 | 7.433 | 1.504 |
| 2 | 7.408 | 1.168 |
| 3 | 7.399 | 1.044 |

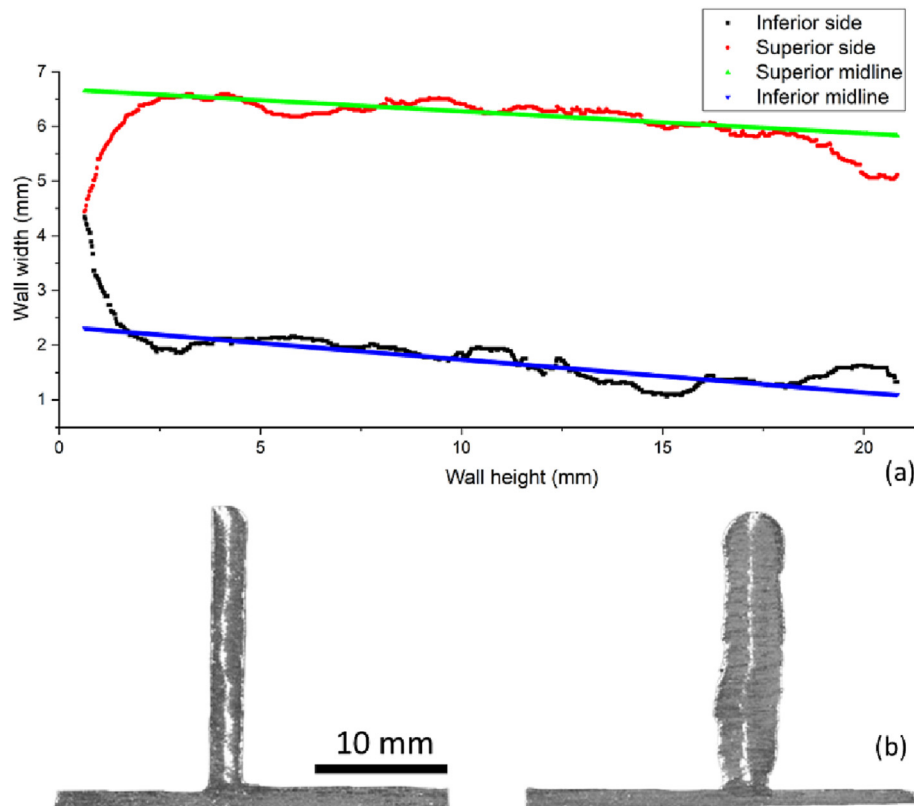


Fig. 4. As-built cross-sections (a) virtual profile and midlines; (b) wall before (right) and after (left) milling.

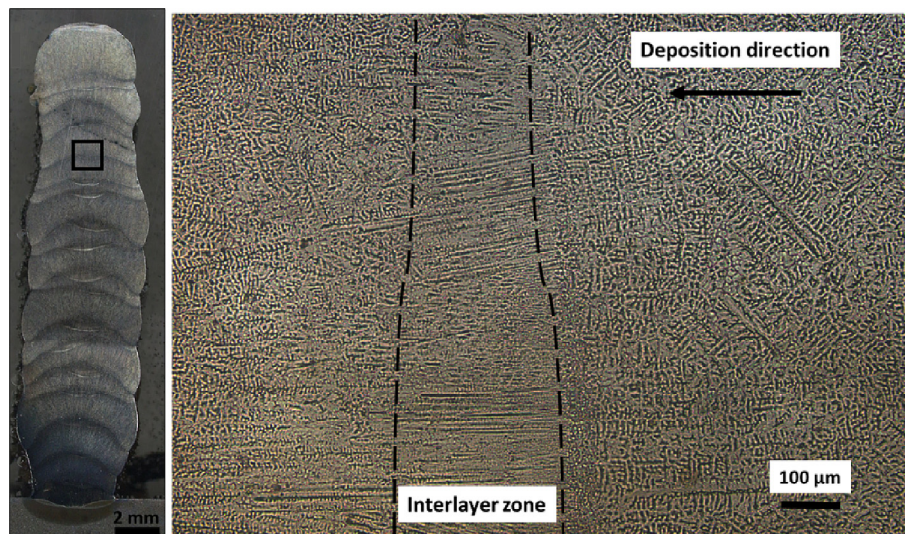


Fig. 5. As-built microstructure. a) Overview of the wall cross-section; b) representative micrograph of central region of the as-built material (black square in a).

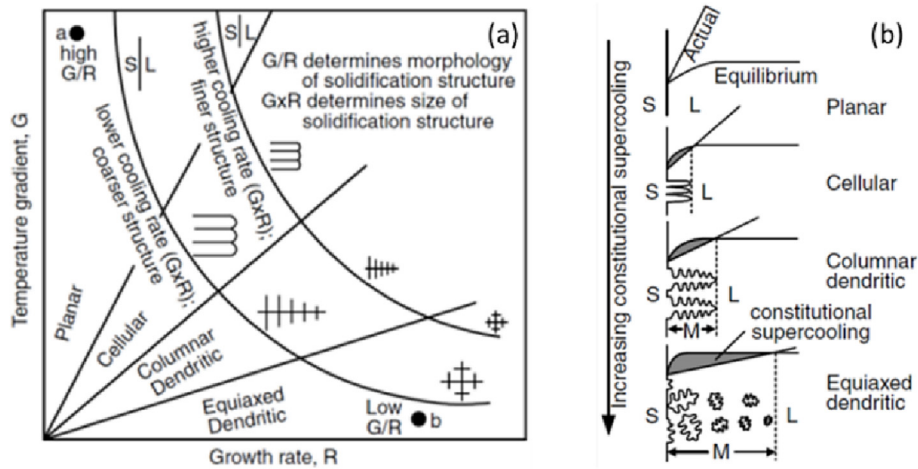


Fig. 6. (a) Effect of the temperature gradient, G , and growth rate, R , on the morphology and size of solidification structures. (b) Effect of constitutional supercooling on the solidification mode. Obtained from [53].

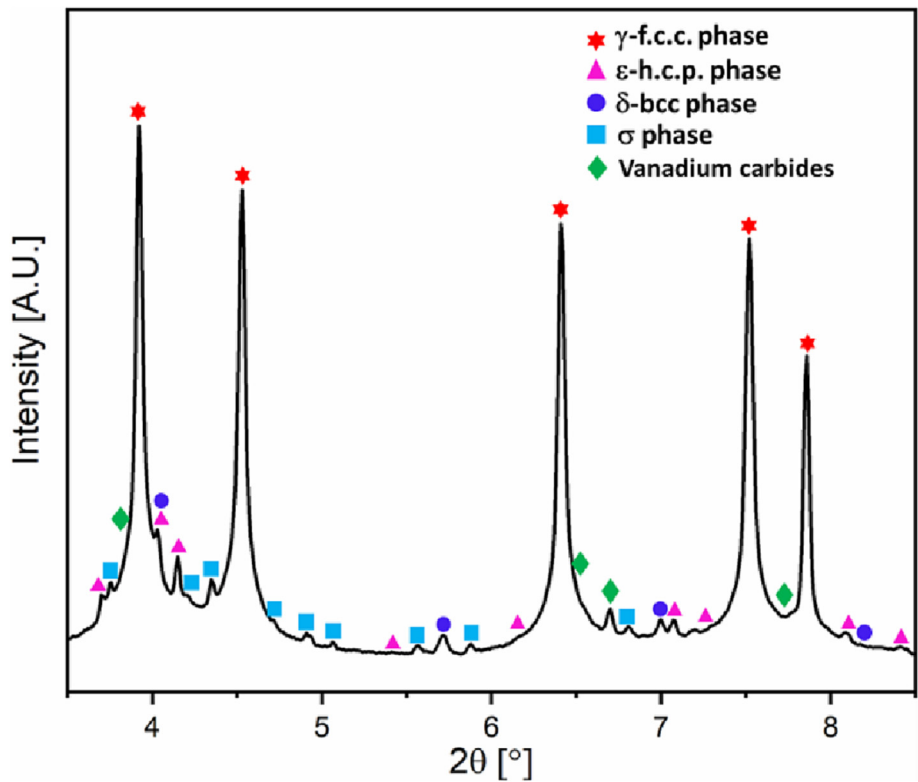


Fig. 7. Synchrotron X-ray diffraction pattern of the as-deposited sample.

Table 4
Phase volume fraction determined by SXRD for as-built sample.

| Sample | Volume fraction (%) |
|------------------------|---------------------|
| FCC - γ phase | 93.48 |
| HCP - ϵ phase | 1.36 |
| BCC - δ phase | 3.21 |
| σ phase | 1.15 |
| Vanadium carbides | 0.80 |

ogy may arise, as well as the formation of defects and deviations. These factors can negatively impact the accuracy of fabrication

and the uniformity of the deposited wall [48]. Moreover, the large heat source dimensions that feature wire and arc additive manufacturing always render the development of waviness values above those obtained with other types of heat sources such as lasers or electron beams. Fig. 4 (a) depicts the virtually reconstructed profile and the respective midlines that served as reference for the parameter's calculation. The waviness level of the as-built wall was considered low and comparable to other arc-based AM processes where higher resolution is generally reached [49]. The deposition efficiency was determined to be 53% by comparing the cross-sectional area before and after milling, as shown in Fig. 4 (b). This value was deemed appropriate for a first deposition. Porosity was analyzed by means of the volume of voids (VV) method, calculated

by comparison of the density of the deposited material and that of the used feedstock material, and these results are depicted in Table 3. Based on the measured data, it can be inferred that the produced part was homogenous and continuous, as the volume of voids (VV) for all the tested samples was found to be less than 1.5%. This is an encouraging result that could help in reducing the occurrence of such imperfections in components manufactured via arc-based additive manufacturing. [50]. This is further sup-

ported by the absence of visible pores or cracks, as shown in Fig. 4 (b).

3.1. Microstructural characterization

The as-built microstructure was first characterized by optical microscopy. Micrographs taken from the bottom, center e top regions of the wall cross-section were analyzed, revealing a consis-

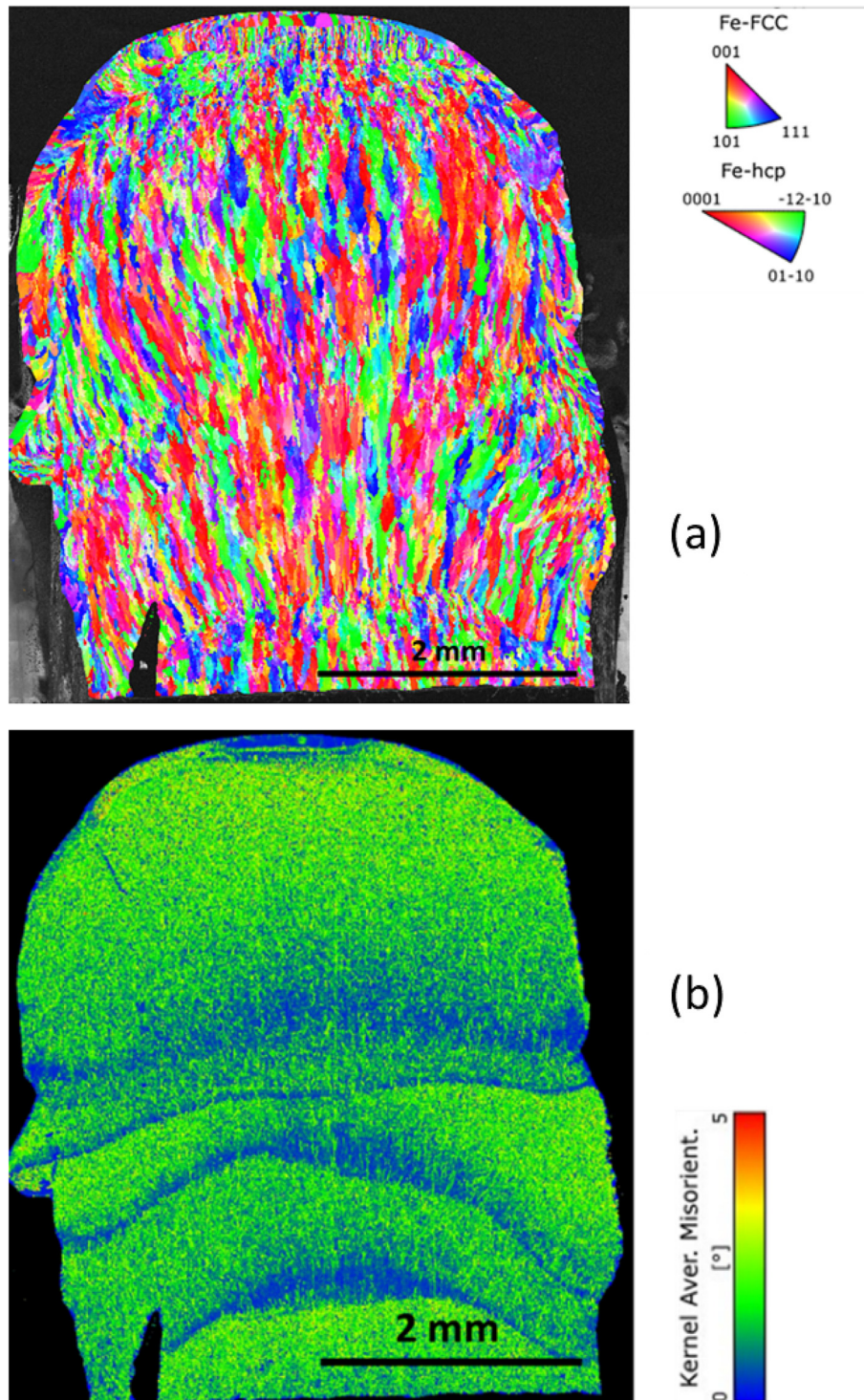


Fig. 8. (a) EBSD map and (b) KAM's color map of the WAAMed Fe-SMA sample.

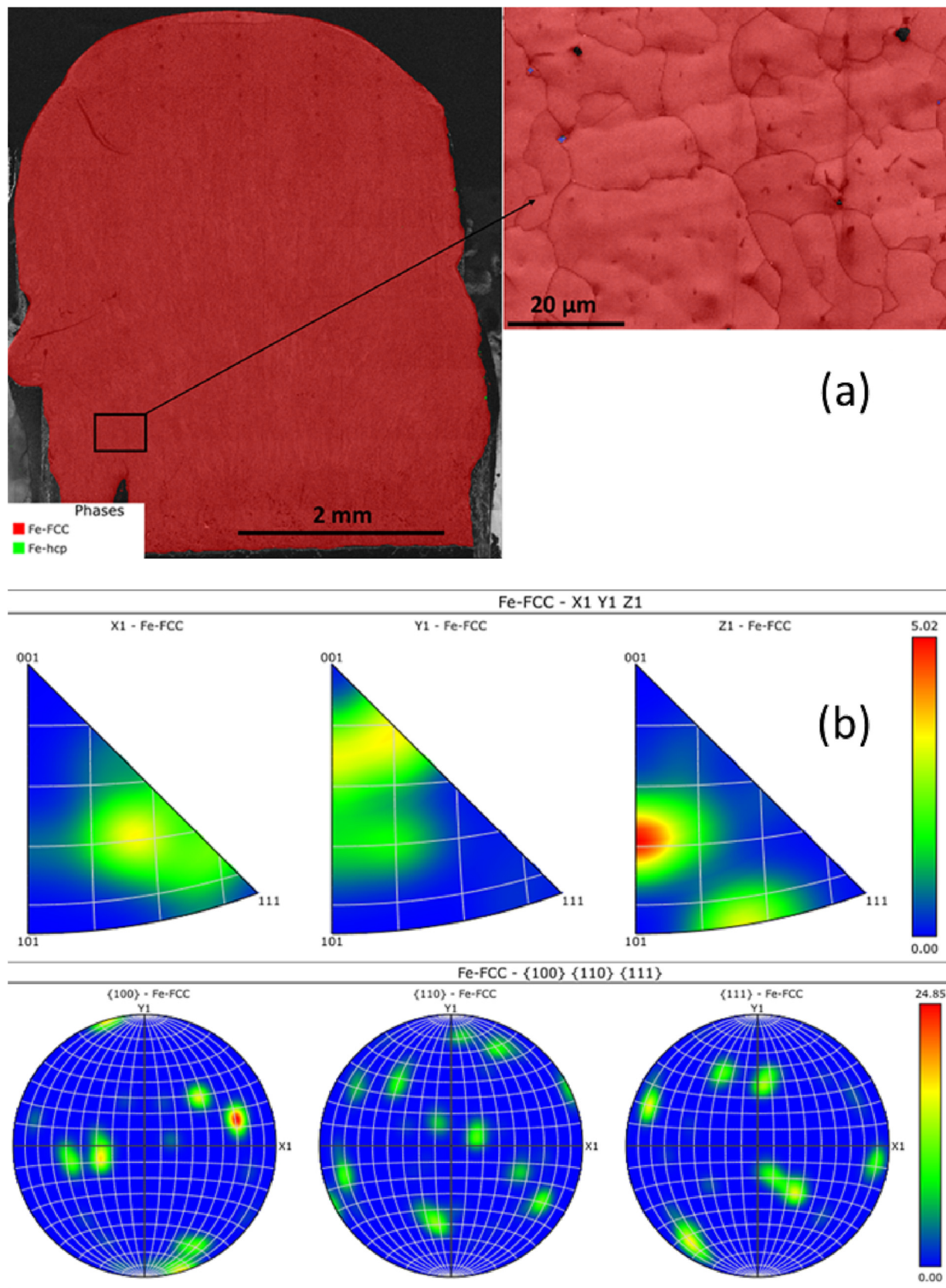


Fig. 9. (a) Phase identification map, highlighting the primary γ phase (red), with trace amounts of ε phase (blue). (b) Inverse pole figures for the γ phase. (For interpretation of the references to color in this figure legend, the reader is referred to the web version of this article.)

tent, similar and uniform microstructural, as depicted in Fig. 5. The as-deposited structure exhibited a columnar dendritic grain morphology, with a directional growth pattern at the layer interfaces resulting from the solidification path. The microstructure size and morphology during solidification are mainly governed by the temperature gradient (G) and growth rate (R) relationship. The cooling rate is determined by the product $G \times R$, while the G/R ratio affects the solidification mode. High energy density processes like WAAM lead to the formation of columnar grains due to epitaxial solidification in the direction of the strongest thermal gradient, which typically coincides with the building direction, owing to the high temperature gradient and rapid cooling rates during solidification. [32,51]. Also, columnar grains were observed by Ke et al. [38] when a constant current was used for a GTAW-based WAAM-DED process. Since the material being deposited has the same composition of the previous layer (except near the substrate), grain growth is supported by the previously solidified microstructure. Also, the number of grains within a layer tends to remain constant as the solidification occurs by lengthening the dendrites and dendrite arm enlargement [52]. Fig. 6 presents the effect of temperature gradient and growth rate on the morphology and size of the solidification structures and the columnar dendritic region can be defined as a moderate low G/R ratio. Also, this morphology is even more noticed with the increase of the constitutional super-

Table 5

As deposited Fe-SMA Average composition as measured by SEM/EDS.

| Element | Wt.% | Wt.% Sigma |
|---------|-------|------------|
| C | 8.40 | 0.04 |
| Si | 4.39 | 0.01 |
| V | 0.71 | 0.01 |
| Cr | 9.39 | 0.01 |
| Mn | 14.86 | 0.02 |
| Fe | 58.18 | 0.03 |
| Ni | 4.07 | 0.02 |

Table 6

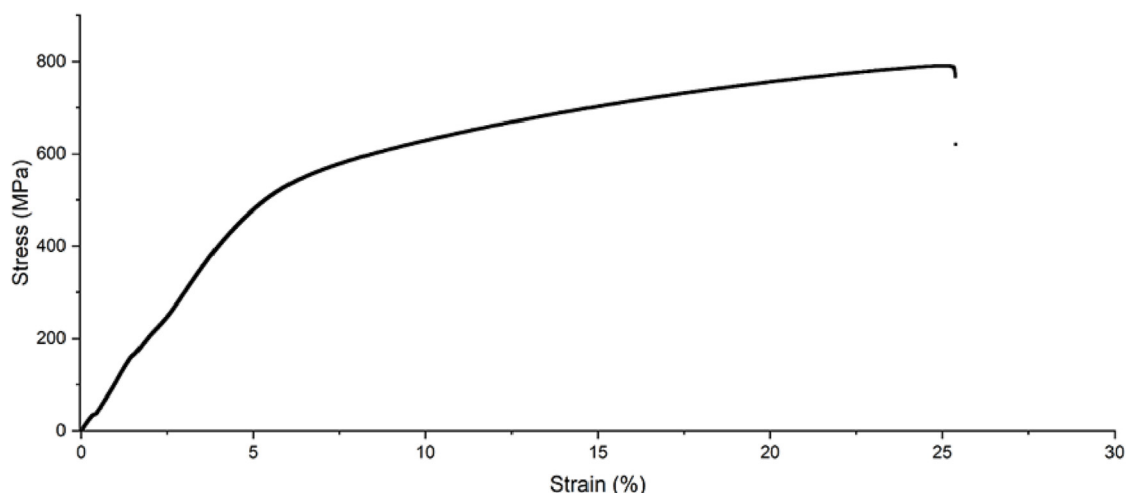
Average mechanical properties obtained with tensile testing.

| | |
|-----------------|--------------|
| Yield strength | 472 ± 18 MPa |
| Fracture stress | 821 ± 64 MPa |
| Elongation | 26 ± 1.5 % |

cooling, which leads to an enlargement of the solid (S) - liquid (L) interface, known as mushy zone (M) [52,53].

A representative diffraction pattern (Fig. 7) was obtained via synchrotron X-ray diffraction analysis of the sample. The results indicate that the γ phase is the primary constituent of the as-deposited material. Additionally, minor peaks attributed to VC precipitates, ϵ phase, and intermetallic σ phase were also detected. Koster et al. [54] assumed that the residual stress in the vicinity of the VC particles, caused by the lattice mismatch between coherent VC particles and the γ matrix, led to the formation of ϵ phase in this same alloy without the need for external deformation to be imposed. The formation of the σ phase is associated with the low diffusivity of Cr and Si, which promotes its formation during solidification and cooling. Although Cr can be decisive in forming the brittle σ phase (when exceeds 7 wt%), which impedes SME, it is often used to improve the material corrosion resistance. To avoid massive formation of σ phase formation, the addition of Ni to the alloy composition is found to be one of the most effective methods [55]. Table 4 presents the phase volume fraction as determined by SXRD.

Fig. 8 (a) depicts the EBSD results performed on a top representative region of the Fe-SMA WAAMed sample. The computational analysis of the complete image counted the presence of 4683 grains, with an average grain size of 56.5 μm and predominantly columnar. The top and side regions of the wall exhibit a finer grain structure compared to the central area. This phenomenon is attributed to the higher cooling rates ($G \times R$) experienced by the external regions due to their direct exposure to the environment. Consequently, these regions display more refined solidification structures [53], which aligns with existing research findings as illustrated in Fig. 6. Moreover, the analyzed region demonstrated an average value of 1.4° for the Kernel Average Misorientation (KAM). The KAM distribution is a valuable tool for inferring on the geometrical necessary dislocation (GND) density distribution across the material. In the case of grains that have undergone deformation, the KAM tends to be higher, usually surpassing 1° , owing to the presence of a greater dislocation density. In contrast, recrystallized grains tend to exhibit lower KAM values, often below 1° [56,57]. In Fig. 8 (b) the KAM distribution is visually represented through a color map, indicating lower KAM values in the areas along the fusion lines and borders (represented by the blue color). These regions correspond to areas with lower dislocation density, and it can be associated to the local high cooling rates experienced during the deposition process. Conversely, green and yellow colors represent regions with higher dislocation density, suggesting the

**Fig. 10.** Representative tensile behavior of the as-built WAAM Fe-SMA.

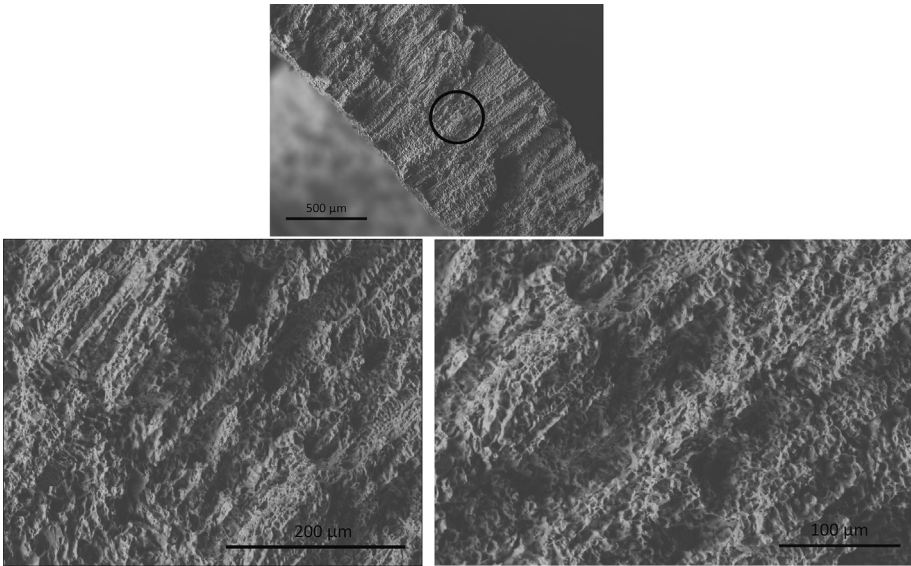


Fig. 11. SEM image with different magnifications of the specimen's fracture surface after tensile testing.

accommodation of residual deformation, possibly induced by the multiple non-equilibrium thermal cycles that occur within the material. An intensification in the dislocation density results in a high amount of dislocation interactions and entanglements, as well as a reduction in the mean free path of dislocations. This effect ultimately impacts the strength and functionally of Fe-SMA [58,59]. Evidently, as previously shown by optical microscopy (Fig. 5), the formation of columnar grains along the built direction can be noticed (refer to Fig. 8). This morphology is accentuated in AM due to the absence of a nucleation barrier, owing to the epitaxial

Table 7
Sample phase volume fraction after tensile test determined by SXRD.

| Sample | Volume fraction (%) |
|------------------------|---------------------|
| FCC - γ phase | 61.49 |
| HCP - ϵ phase | 32.58 |
| BCC - δ phase | 3.93 |
| σ phase | 1.20 |
| Vanadium carbides | 0.80 |

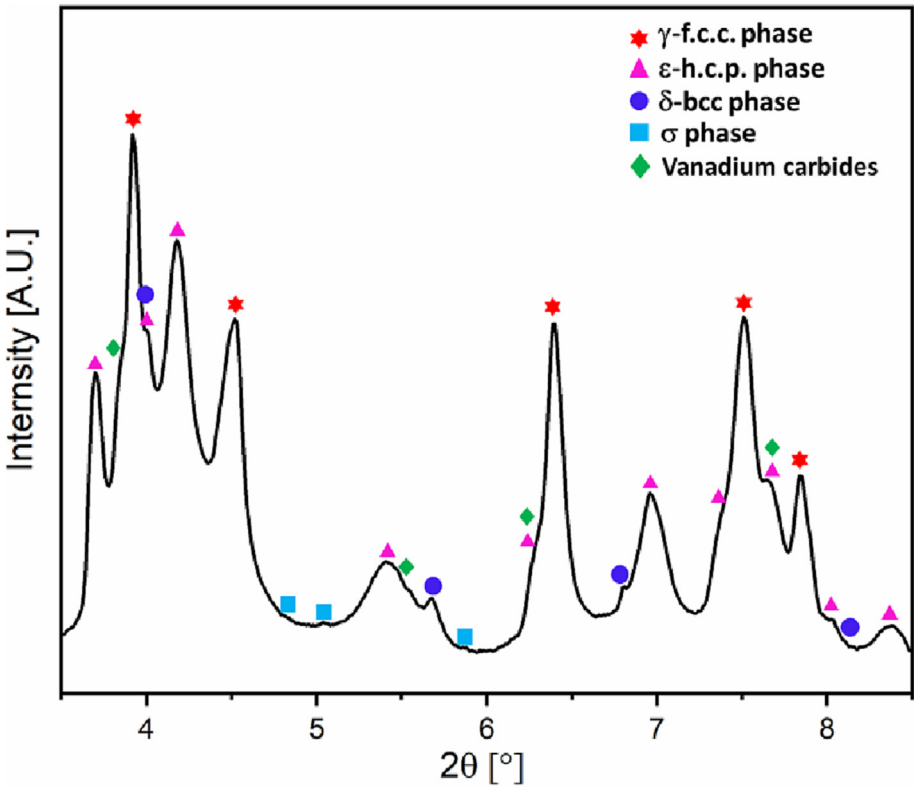


Fig. 12. Synchrotron X-ray diffraction pattern of the Fe-SMA material after tensile test.

growth of each successive layer from the previous one [60]. The process involves localized solidification on a small scale that occurs under significant thermal gradients (G) with high cooling rates (T), which promote the formation of dendritic-columnar structures. Furthermore, equiaxed grains that may form in the final layer (lower G and T) are prone to remelting and solidifying again as columnar grains during the deposition of the subsequent layer [61]. In DED processes, the temperature gradient (G) can reach up to 200 K/mm, coupled with solidification rates (R) that result in cooling rates between 102 and 103 K/s, thereby favoring the formation of columnar grains due to the direction of heat transfer [62]. The grains growth in this direction is facilitated as their growth velocity is significantly higher when the crystal growth direction aligns with the maximum temperature gradient. The microstructure evolution is predominantly influenced by the ratio G/R . At the bottom of the melt pool, the highest value of G is observed due to decreasing heat input, and R is very low as well. Hence, G/R attains a large value [63]. For Fe-SMA alloys with low stacking fault energy (SFE), FCC (γ) and HCP (ϵ) phases are stable [64], and the aspects of the γ - ϵ transformation in Fe-SMA with low SFE were already presented by Xu [65]. The high mechanical properties exhibited by Fe-based SMA alloys, as will be evidenced in section 3.2 (Table 6), are associated to a deformation-induced martensitic transformation, from the FCC phase to HCP, during loading, and its reversion can be achieved with subsequent heating [19]. A martensitic transformation from ϵ martensite to α' martensite (with BCC structure) can also occur. However, it has been reported that $\gamma \rightarrow \epsilon \rightarrow \alpha'$ can degrade the SME [66,67]. According to the phase maps showed in Fig. 9 (a), it can be noticed that the microstructure of the as-built Fe-SMA alloy is predominantly composed by γ phase with a very small amount of ϵ phase, which also validates the previously shown synchrotron X-ray diffraction pattern presented in Fig. 7. Also, comparing both analysis technologies, the lower resolution of the EBSD method hindered the identification of other phases, previously detected by SXR, particularly those with very small volume fractions. This showcases the

excellent detection capabilities associated to high energy SXR for advanced materials characterization. As expected, no α' martensite was detected. This result corroborates the recent work of Gu et al. [68] whom stated that a Mn content between 14 and 21 wt% is sufficient to avoid α' martensite formation, which is confirmed by the present work (the percentage of Mn in this work was 17 wt%) and Zhang et al [69]. The phase identification maps, inverse pole figures (IPF) and pole figures in a partially amplified area are depicted Fig. 9.

Data of EDS analysis of the as-deposited material is presented in Table 5 and indicates a minor reduction in the elemental concentration when compared to the raw material, except for nickel, which exhibited a near constant level. This outcome suggests the occurrence of elemental evaporation during the process, which was particularly prominent for manganese. The mass percentage loss in the alloy composition for manganese was quantified at $\approx 2.1\%$. This observation may be attributed to the lower boiling temperature of Mn, when compared to the other alloying elements that compose the present Fe-SMA.

3.2. Mechanical characterization

The mechanical properties of the as-deposited material were assessed through tensile testing at room temperature. Fig. 10 depicts a representative stress-strain curve of the as-deposited specimen. The average yield strength at 0.2% strain, fracture stress (referred to as ultimate tensile strength), and elongation are detailed in Table 6. Overall, all samples exhibit a high strength (over 700 MPa of fracture stress) and excellent ductility ($>25\%$ of elongation). This indicates that the application of an arc-based additive manufacturing technique for the production of Fe-SMA components does not compromise their mechanical properties, even in the as-deposited state. Necking was not discerned in the specimens during the tensile testing, which is evident from the characteristic stress-strain curve depicted in Fig. 10. The fracture was observed right after the strain hardening regime. SEM imaging

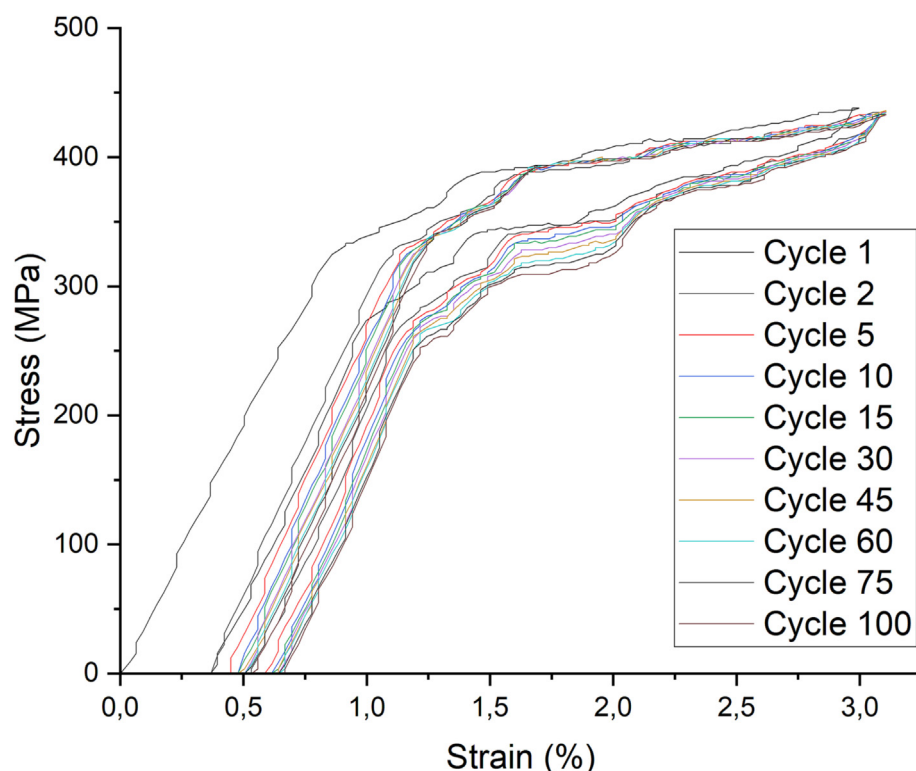


Fig. 13. Cycling behavior of Fe-SMA specimen.

of the fracture surfaces after tensile testing reveals the presence of dimples along the fracture surface (Fig. 11), indicating a ductile-like fracture mode that is consistent with the high material elongation prior to fracture. The tensile load promoted the expected $\gamma \rightarrow \varepsilon$ phase transformation, which is a key microstructural behavior of this Fe-SMA. The increased volume fraction of ε martensite at the expense of γ austenite was confirmed by the synchrotron X-ray diffraction pattern of the material after the tensile test (Fig. 12). The volume fractions of VC and σ -phase remained in the microstructure (refer to Table 7).

The superelastic behavior of shape memory alloys (SMAs) has recently been investigated for its potential in seismic-resistant structures to reduce residual deformations. SMAs have the ability to dissipate energy while retaining their original shape without permanent deformation. Although it was known that Fe-SMA, in general, offered negligible SE [21], recent studies demonstrated that large elastic strain fields form near the VC precipitates, improving the SE (and also SME) response in the Fe-17Mn-5Si-10Cr-4Ni-1(V, C) alloy. Besides, special textures can lead to the same improvement [1]. It is essential to develop high damping capacity materials, enhancing the SE behavior of Fe-SMAs, in a way that this material can turn into an alternative for seismic purposes. To evaluate the viability of using Fe-SMAs in these applications, it is crucial to assess their load/unload cycling behavior and repeatability. In this study, the as-deposited material was subjected to a cycling routine to evaluate its SE properties, and it

was subjected to a cycling routine, where it was loaded up to a maximum imposed strain of 3% and then unloaded to a zero-stress condition. Fig. 13 depicts some of the 100 load/unload cycles performed for both the Fe-SMA specimen. After the second cycle, a 0.60 to 0.67% irreversible strain was measured, and from the fifth cycle onwards, all cycles showed a similar cyclic behavior, indicating excellent stability. The results were confirmed through graphs showing a constant irrecoverable strain and maximum stress as a function of the number of load/unload cycles (Fig. 14). In Fig. 14 (c), a considerable higher absorbed energy is noted in the first load/unload solicitation due to the higher irrecoverable strain [70], that can be caused by lower SE recovery. This absorbed energy is converted to heat, resulting in thermal softening of the material and consequently a reduction in the SE [71]. Also, if the absorbed energy surpasses a certain threshold, plastic deformation can occur, leading to irreversible changes and a reduction in the SE. The curve stabilized after the first cycle until the 50th cycle, where a slight reduction in the measured values was detected, which may be associated with martensite stabilization.

To obtain microhardness measurements, five continuous lines were indented horizontally at a distance of 200 μm , as shown in Fig. 15 (top). Line L3 represented the centerline, with a distance of 0.75 mm from lines L2 and L4 and 1.35 mm from lines L1 and L5. The average microhardness line across the cross-section was determined, along with its standard deviation range (i.e., upper, and lower limits), as depicted in Fig. 15 (bottom). The measured

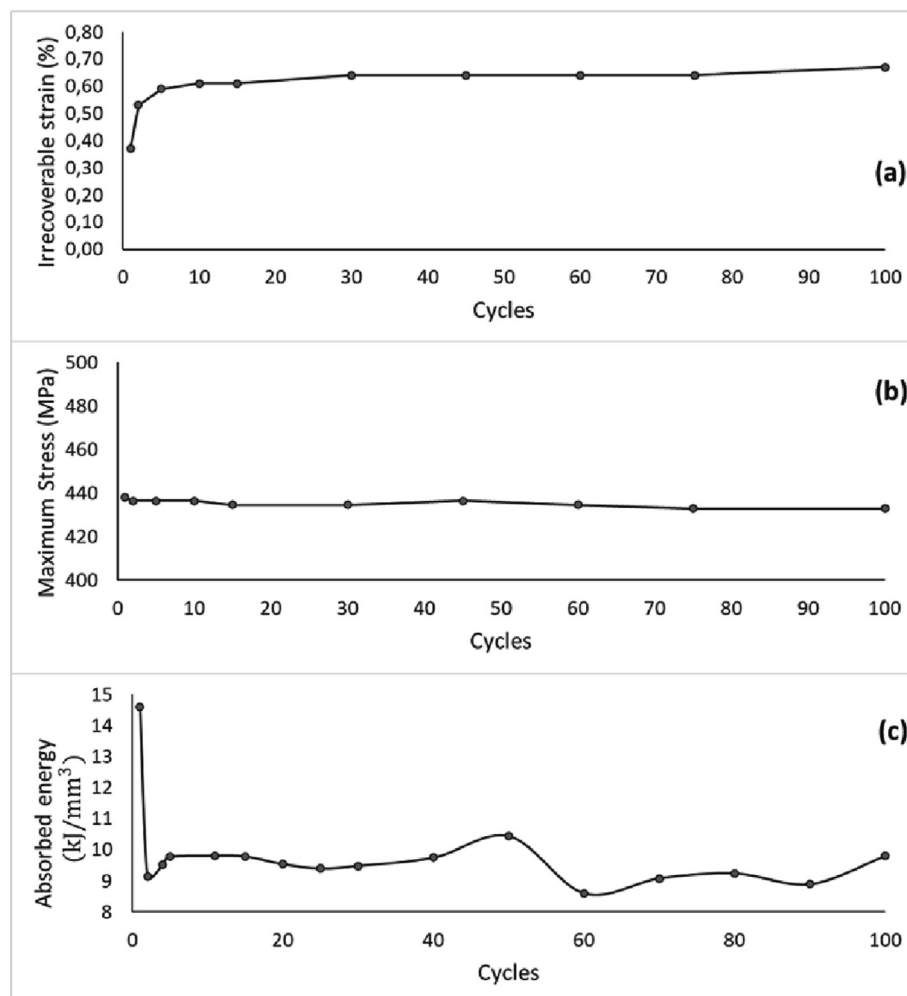


Fig. 14. Evolution of the (a) irrecoverable strain; (b) maximum stress; and absorbed energy with the number of cycles.

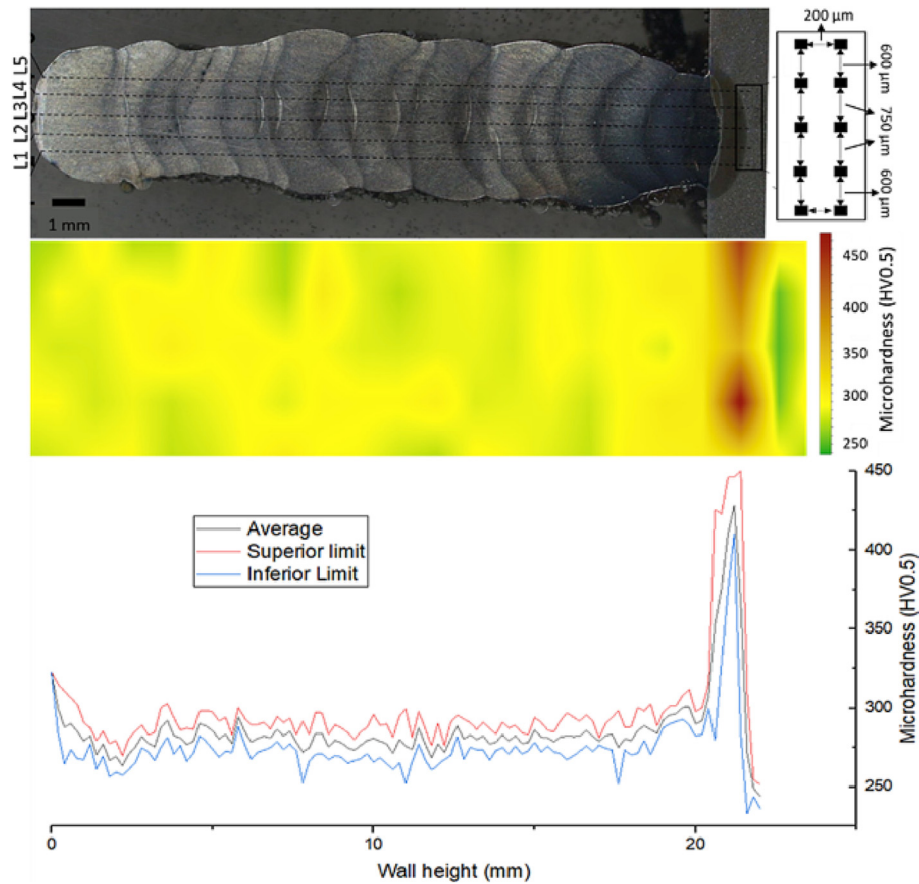


Fig. 15. Microhardness measurements: measured lines on the wall cross-section (top); intensity map (middle); average measurements and limits according to standard deviation.

values show a nearly constant and horizontal pattern between 250 and 300 $HV_{0.5}$, with minor oscillations and a slight increase on the upper section of the wall, displayed on the left region of Fig. 15. This phenomenon can be attributed to the presence of finer grains in the border area, which enhances this mechanical property due to the Hall-Petch effect [72]. Along the substrate zone, the hardness levels increase over 400 $HV_{0.5}$. This is attributed to a dilution effect caused by mixing the Fe-SMA feedstock material with the substrate used for deposition. Therefore, the deposited material, along its useful region, presents the important characteristic of microstructural uniformity and homogeneity, as represented by these microhardness values. The predominance of green and yellow shades in the color map, as seen in Fig. 15 (middle), confirms this trend, except for the substrate area where higher hardness (indicated by the red color) was observed.

4. Conclusions

In this study, a pioneer application of a Fe-SMA in arc-based DED additive manufacturing was successfully accomplished and the resulting fabricated component was characterized in terms of microstructure, mechanical and functional behavior. The single wall produced had low porosity and a high deposition efficiency (53%), resulting in reduced surface waviness and less material removal during post-deposition processes such as machining and finishing. The microstructure of the as-deposited material was predominantly composed of the high temperature γ phase (>93%) with trace amounts of VC, ϵ (<1.5%) and σ phases, which were not detrimental to the material mechanical performance. The

solidification process and inherent heat flux in high heat input AM processes led to a columnar dendritic morphology. The yield strength (472 MPa), fracture stress (821 MPa) and elongation (26%) revealed excellent mechanical performance enabling the use of the material and process in construction applications. Tensile testing revealed a $\gamma \rightarrow \epsilon$ phase transformation, with the volume fraction of γ and ϵ phases shifting to over 61% and 32%, respectively. Additionally, cyclic testing demonstrated repeatable mechanical response and high absorbed energy, maximum stress, and low irrecoverable strain, further highlighting the material's potential for use in civil engineering applications, such as in seismic systems.

Data availability

Data will be made available on request.

Declaration of Competing Interest

The authors declare that they have no known competing financial interests or personal relationships that could have appeared to influence the work reported in this paper.

Acknowledgments

The authors acknowledge Fundação para a Ciência e a Tecnologia (FCT-MCTES) for its financial support via the project UIDB/00667/2020 (UNIDEMI). JS acknowledges the China Scholarship Council for funding the Ph.D. grant (CSC NO. 201808320394).

JPO acknowledges funding by national funds from FCT - Fundação para a Ciência e a Tecnologia, I.P., in the scope of the projects LA/P/0037/2020, UIDP/50025/2020 and UIDB/50025/2020 of the Associate Laboratory Institute of Nanostructures, Nanomodelling and Nanofabrication – i3N. This activity has received funding from the European Institute of Innovation and Technology (EIT) – Project Smart WAAM: Microstructural Engineering and Integrated Non-Destructive Testing. This body of the European Union receives support from the European Union's Horizon 2020 research and innovation programme.

References

- [1] M. Mohri, I. Ferretto, C. Leinenbach, D. Kim, D.G. Lignos, E. Ghafoori, Effect of thermomechanical treatment and microstructure on pseudo-elastic behavior of Fe–Mn–Si–Cr–Ni–(V, C) shape memory alloy, *Mater. Sci. Eng. A* 855 (2022), <https://doi.org/10.1016/j.msea.2022.143917> 143917.
- [2] J. Vůjtek, P. Ryjáček, J. Campos Matos, E. Ghafoori, Iron-Based shape memory alloy for strengthening of 113-Year bridge, *Eng. Struct.* 248 (2021) 113231.
- [3] D.I.H. Rosa, A. Hartloper, A. de Castro e Sousa, D.G. Lignos, M. Motavalli, E. Ghafoori, Experimental behavior of iron-based shape memory alloys under cyclic loading histories, *Constr. Build. Mater.* 272 (2021) 121712.
- [4] J.P. Oliveira, R.M. Miranda, F.M. Braz Fernandes, Welding and joining of NiTi shape memory alloys: a review, *Prog. Mater. Sci.* 88 (2017) 412–466, <https://doi.org/10.1016/j.pmatsci.2017.04.008>.
- [5] J. van Humbeeck, Non-medical applications of shape memory alloys, *Mater. Sci. Eng. A* 273–275 (1999) 134–148, [https://doi.org/10.1016/S0921-5093\(99\)00293-2](https://doi.org/10.1016/S0921-5093(99)00293-2).
- [6] K. Otsuka, X. Ren, Physical metallurgy of Ti–Ni-based shape memory alloys, *Prog. Mater. Sci.* 50 (2005) 511–678, <https://doi.org/10.1016/j.pmatsci.2004.10.001>.
- [7] F.G. Askari-Naeini, M. Taghizadeh, M. Mohri, M. Nili-Ahmadabadi, On the microstructure and mechanical properties of a two-way shape memory NiTi/NiTiCu bi-layer diaphragm, *Mater. Des.* 188 (2020), <https://doi.org/10.1016/j.matdes.2019.108464> 108464.
- [8] H. Tamai, Y. Kitagawa, Pseudoelastic behavior of shape memory alloy wire and its application to seismic resistance member for building, *Comput. Mater. Sci.* 25 (2002) 218–227, [https://doi.org/10.1016/S0927-0256\(02\)00266-5](https://doi.org/10.1016/S0927-0256(02)00266-5).
- [9] S. Saadat, M. Noori, H. Davoodi, Z. Hou, Y. Suzuki, A. Masuda, Using NiTi SMA tendons for vibration control of coastal structures, *Smart Mater. Struct.* 10 (2001) 695–704, <https://doi.org/10.1088/0964-1726/10/4/313>.
- [10] E. Ghafoori, E. Hosseini, C. Leinenbach, J. Michels, M. Motavalli, Fatigue behavior of a Fe–Mn–Si shape memory alloy used for prestressed strengthening, *Mater. Des.* 133 (2017) 349–362, <https://doi.org/10.1016/j.matdes.2017.07.055>.
- [11] A. Sato, E. Chishima, K. Soma, T. Mori, Shape memory effect in γ/ϵ transformation in Fe–30Mn–1Si alloy single crystals, *Acta Metall.* 30 (1982) 1177–1183, [https://doi.org/10.1016/0001-6160\(82\)90011-6](https://doi.org/10.1016/0001-6160(82)90011-6).
- [12] T. Maruyama, H. Kubo, Ferrous (Fe-based) shape memory alloys (SMAs): properties, processing and applications, in: *Shape Memory and Superelastic Alloys*, Elsevier, 2011: pp. 141–159. doi: 10.1533/9780857092625.2.141.
- [13] A. Cladera, B. Weber, C. Leinenbach, C. Czaderski, M. Shahverdi, M. Motavalli, Iron-based shape memory alloys for civil engineering structures: an overview, *Constr. Build. Mater.* 63 (2014) 281–293, <https://doi.org/10.1016/j.conbuildmat.2014.04.032>.
- [14] M.R. Izadi, E. Ghafoori, M. Shahverdi, M. Motavalli, S. Maalek, Development of an iron-based shape memory alloy (Fe–SMA) strengthening system for steel plates, *Eng. Struct.* 174 (2018) 433–446, <https://doi.org/10.1016/j.engstruct.2018.07.073>.
- [15] Z.-X. Zhang, J. Zhang, H. Wu, Y. Ji, D.D. Kumar, Iron-based shape memory alloys in construction: research, applications and opportunities, *Materials* 15 (2022) 1723, <https://doi.org/10.3390/ma15051723>.
- [16] C. Leinenbach, H. Kramer, C. Bernhard, D. Eifler, Thermo-mechanical properties of an Fe–Mn–Si–Cr–Ni–VC shape memory alloy with low transformation temperature, *Adv. Eng. Mater.* 14 (2012) 62–67, <https://doi.org/10.1002/adem.201100129>.
- [17] K. Li, Z. Dong, Y. Liu, L. Zhang, A newly developed Fe-based shape memory alloy suitable for smart civil engineering, *Smart Mater. Struct.* 22 (4) (2013) 045002.
- [18] W.J. Lee, B. Weber, G. Feltrin, C. Czaderski, M. Motavalli, C. Leinenbach, Phase transformation behavior under uniaxial deformation of an Fe–Mn–Si–Cr–Ni–VC shape memory alloy, *Mater. Sci. Eng. A* 581 (2013) 1–7, <https://doi.org/10.1016/j.msea.2013.06.002>.
- [19] Z. Dong, U.E. Klotz, C. Leinenbach, A. Bergamini, C. Czaderski, M. Motavalli, A novel Fe–Mn–Si shape memory alloy with improved shape recovery properties by VC precipitation, *Adv. Eng. Mater.* 11 (2009) 40–44, <https://doi.org/10.1002/adem.200800312>.
- [20] R.A. Rahman, D. Juhre, T. Halle, Review of Applications of Ferrous Based Shape Memory Smart Materials in Engineering and in Biomedical Sciences, 2019.
- [21] M.A. Molod, P. Spyridis, F.-J. Barthold, Applications of shape memory alloys in structural engineering with a focus on concrete construction – a comprehensive review, *Constr. Build. Mater.* 337 (2022), <https://doi.org/10.1016/j.conbuildmat.2022.127565> 127565.
- [22] I. Ferretto, D. Kim, M. Mohri, E. Ghafoori, W.J. Lee, C. Leinenbach, Shape recovery performance of a (V, C)-containing Fe–Mn–Si–Cr shape memory alloy fabricated by laser powder bed fusion, *J. Mater. Res. Technol.* 20 (2022) 3969–3984, <https://doi.org/10.1016/j.jmrt.2022.08.143>.
- [23] T.Y. Hsu, X. Zuyao, Martensitic transformation in Fe–Mn–Si based alloys, *Mater. Sci. Eng. A* 273–275 (1999) 494–497, [https://doi.org/10.1016/S0921-5093\(99\)00386-X](https://doi.org/10.1016/S0921-5093(99)00386-X).
- [24] W. Wang, L. Li, A. Hosseini, E. Ghafoori, Novel fatigue strengthening solution for metallic structures using adhesively bonded Fe–SMA strips: A proof of concept study, *Int. J. Fatigue* 148 (2021), <https://doi.org/10.1016/j.ijfatigue.2021.106237> 106237.
- [25] A. Arabi-Hashemi, W.J. Lee, C. Leinenbach, Recovery stress formation in FeMnSi based shape memory alloys: impact of precipitates, texture and grain size, *Mater. Des.* 139 (2018) 258–268, <https://doi.org/10.1016/j.matdes.2017.11.006>.
- [26] X. Yang, Y. Zhang, Prediction of high-entropy stabilized solid-solution in multi-component alloys, *Mater. Chem. Phys.* 132 (2012) 233–238, <https://doi.org/10.1016/j.matchemphys.2011.11.021>.
- [27] C. Leinenbach, A. Arabi-Hashemi, W.J. Lee, A. Lis, M. Sadegh-Ahmadi, S. van Petegem, T. Panzner, H. van Swygenhoven, Characterization of the deformation and phase transformation behavior of VC-free and VC-containing FeMnSi-based shape memory alloys by in situ neutron diffraction, *Mater. Sci. Eng. A* 703 (2017) 314–323, <https://doi.org/10.1016/j.msea.2017.07.077>.
- [28] J.P. Oliveira, T.G. Santos, R.M. Miranda, Revisiting fundamental welding concepts to improve additive manufacturing: from theory to practice, *Prog. Mater. Sci.* 107 (2020) 100590.
- [29] B. Dutta, Directed energy deposition (DED) technology, in: *Encyclopedia of Materials: Metals and Alloys*, Elsevier, 2022, pp. 66–84.
- [30] Y. Zhang, W. Jarosinski, Y.-G. Jung, J. Zhang, Additive manufacturing processes and equipment, in: *Addit. Manuf.*, Elsevier, 2018, pp. 39–51. 10.1016/B978-0-12-812155-9.00002-5.
- [31] D. Delgado Camacho, P. Clayton, W.J. O'Brien, C. Seepersad, M. Juenger, R. Ferron, S. Salamone, Applications of additive manufacturing in the construction industry – a forward-looking review, *Autom. Constr.* 89 (2018) 110–119, <https://doi.org/10.1016/j.autcon.2017.12.031>.
- [32] A.N. Alagha, S. Hussain, W. Zaki, Additive manufacturing of shape memory alloys: A review with emphasis on powder bed systems, *Mater. Des.* 204 (2021) 109654.
- [33] M. Shahverdi, S. Raza, E. Ghafoori, C. Czaderski, J. Michels, M. Motavalli, Recent advancements in development and application of an iron-based shape memory alloy at Empa, *Chimia (Aarau)* 76 (2022) 242, <https://doi.org/10.2533/chimia.2022.242>.
- [34] D. Kim, I. Ferretto, C. Leinenbach, W. Lee, 3D and 4D printing of complex structures of Fe–Mn–Si-Based shape memory alloy using laser powder bed fusion, *Adv. Mater. Interfaces* 9 (2022) 2200171, <https://doi.org/10.1002/admi.202200171>.
- [35] I. Ferretto, D. Kim, N.M. Della Ventura, M. Shahverdi, W. Lee, C. Leinenbach, Laser powder bed fusion of a Fe–Mn–Si shape memory alloy, *Addit. Manuf.* 46 (2021) 102071.
- [36] X. Yang, L. Cheng, H. Peng, B. Qian, L. Yang, Y. Shi, A. Chen, Z. Zhang, L. Zhao, N. Hu, C. Yan, Y. Shi, Development of Fe–Mn–Si–Cr–Ni shape memory alloy with ultrahigh mechanical properties and large recovery strain by laser powder bed fusion, *J. Mater. Sci. Technol.* 150 (2023) 201–216, <https://doi.org/10.1016/j.jmst.2022.11.046>.
- [37] Z. Zeng, B.Q. Cong, J.P. Oliveira, W.C. Ke, N. Schell, B. Peng, Z.W. Qi, F.G. Ge, W. Zhang, S.S. Ao, Wire and arc additive manufacturing of a Ni-rich NiTi shape memory alloy: Microstructure and mechanical properties, *Addit. Manuf.* 32 (2020), <https://doi.org/10.1016/j.addma.2020.101051> 101051.
- [38] W.C. Ke, J.P. Oliveira, B.Q. Cong, S.S. Ao, Z.W. Qi, B. Peng, Z. Zeng, Multi-layer deposition mechanism in ultra high-frequency pulsed wire arc additive manufacturing (WAAM) of NiTi shape memory alloys, *Addit. Manuf.* 50 (2022), <https://doi.org/10.1016/j.addma.2021.102513> 102513.
- [39] J.P. Oliveira, A.J. Cavaleiro, N. Schell, A. Stark, R.M. Miranda, J.L. Ocana, F.M. Braz Fernandes, Effects of laser processing on the transformation characteristics of NiTi: A contribute to additive manufacturing, *Scr. Mater.* 152 (2018) 122–126, <https://doi.org/10.1016/j.scriptamat.2018.04.024>.
- [40] L.J. da Silva, D.M. Souza, D.B. de Araújo, R.P. Reis, A. Scotti, Concept and validation of an active cooling technique to mitigate heat accumulation in WAAM, *Int. J. Adv. Manuf. Technol.* 107 (2020) 2513–2523, <https://doi.org/10.1007/s00170-020-05201-4>.
- [41] E.A. Alberti, B.M.P. Bueno, A.S.C.M. D'Oliveira, Processamento de Ligas de Níquel com Técnica de Manufatura Aditiva Utilizando Plasma por Arco Transferido, *Soldagem & Inspeção*. 20 (2015) 137–147, <https://doi.org/10.1590/0104-9224/SI2002.02>.
- [42] J. Wang, Z. Pan, G. Yang, J. Han, X. Chen, H. Li, Location dependence of microstructure, phase transformation temperature and mechanical properties on Ni-rich NiTi alloy fabricated by wire arc additive manufacturing, *Mater. Sci. Eng. A* 749 (2019) 218–222, <https://doi.org/10.1016/j.msea.2019.02.029>.
- [43] J. Xiong, Y.-J. Li, Z.-Q. Yin, H. Chen, Determination of surface roughness in wire and arc additive manufacturing based on laser vision sensing, *Chinese J. Mechan. Eng.* 31 (2018) 74, <https://doi.org/10.1186/s10033-018-0276-8>.
- [44] J. Xiong, Y. Li, R. Li, Z. Yin, Influences of process parameters on surface roughness of multi-layer single-pass thin-walled parts in GMAW-based

- additive manufacturing, *J. Mater. Process Technol.* 252 (2018) 128–136, <https://doi.org/10.1016/j.jmatprotec.2017.09.020>.
- [45] A.B. Spierings, M. Schneider, R. Eggenberger, Comparison of density measurement techniques for additive manufactured metallic parts, *Rapid Prototyp. J.* 17 (2011) 380–386, <https://doi.org/10.1108/13552541111156504>.
- [46] N. Kashaev, M. Horstmann, V. Ventzke, S. Riekehr, N. Huber, Comparative study of mechanical properties using standard and micro-specimens of base materials Inconel 625, Inconel 718 and Ti-6Al-4V, *J. Mater. Res. Technol.* 2 (2013) 43–47, <https://doi.org/10.1016/j.jmrt.2013.03.003>.
- [47] ISO, ISO 6507-1:2018(en) Metallic materials – Vickers hardness test – Part 1: Test method, 2018.
- [48] H. Cao, R. Huang, H. Yi, M. Liu, L. Jia, Asymmetric molten pool morphology in wire-arc directed energy deposition: evolution mechanism and suppression strategy, *Addit. Manuf.* 59 (2022), <https://doi.org/10.1016/j.addma.2022.103113> 103113.
- [49] H. Geng, J. Li, J. Xiong, X. Lin, D. Huang, F. Zhang, Formation and improvement of surface waviness for additive manufacturing 5A06 aluminium alloy component with GTAW system, *Rapid Prototyp. J.* 24 (2018) 342–350, <https://doi.org/10.1108/RPJ-04-2016-0064>.
- [50] W. Jin, C. Zhang, S. Jin, Y. Tian, D. Wellmann, W. Liu, Wire arc additive manufacturing of stainless steels: a review, *Appl. Sci.* 10 (2020) 1563, <https://doi.org/10.3390/app10051563>.
- [51] R.F. Hamilton, B.A. Bimber, M. Taheri Andani, M. Elahinia, Multi-scale shape memory effect recovery in NiTi alloys additive manufactured by selective laser melting and laser directed energy deposition, *J. Mater. Process Technol.* 250 (2017) 55–64, <https://doi.org/10.1016/j.jmatprotec.2017.06.027>.
- [52] W.' Kurz, D.J.' Fischer, *Fundamentals of Solidification*, Fourth, n.d.
- [53] S. Kou, *Welding Metallurgy*, John Wiley & Sons Inc, Hoboken, NJ, USA, 2002, <https://doi.org/10.1002/0471434027>.
- [54] M. Koster, W.J. Lee, M. Schwarzenberger, C. Leinenbach, Cyclic deformation and structural fatigue behavior of an Fe-Mn-Si shape memory alloy, *Mater. Sci. Eng. A* 637 (2015) 29–39, <https://doi.org/10.1016/j.msea.2015.04.028>.
- [55] H. Otsuka, Fe-Mn-Si based shape memory alloys, *MRS Proc.* 246 (1991) 309, <https://doi.org/10.1557/PROC-246-309>.
- [56] H. Li, E. Hsu, J. Szpunar, H. Utsunomiya, T. Sakai, Deformation mechanism and texture and microstructure evolution during high-speed rolling of AZ31B Mg sheets, *J. Mater. Sci.* 43 (2008) 7148–7156, <https://doi.org/10.1007/s10853-008-3021-3>.
- [57] L. Saraf, Kernel average misorientation confidence index correlation from FIB sliced Ni-Fe-Cr alloy Surface, *Microsc. Microanal.* 17 (2011) 424–425, <https://doi.org/10.1017/S1431927611002996>.
- [58] M.A. Meyers, K.K. Chawla (Eds.), *Mechanical Behavior of Materials*, Cambridge University Press, 2008.
- [59] M. Naeem, H. He, S. Harjo, T. Kawasaki, F. Zhang, B. Wang, S. Lan, Z. Wu, Y. Wu, Z. Lu, C.T. Liu, X.-L. Wang, Extremely high dislocation density and deformation pathway of CrMnFeCoNi high entropy alloy at ultralow temperature, *Scr. Mater.* 188 (2020) 21–25, <https://doi.org/10.1016/j.scriptamat.2020.07.004>.
- [60] M. Bermingham, D. StJohn, M. Easton, L. Yuan, M. Dargusch, Revealing the mechanisms of grain nucleation and formation during additive manufacturing, *JOM* 72 (2020) 1065–1073, <https://doi.org/10.1007/s11837-020-04019-5>.
- [61] T. Özel, H. Shokri, R. Loizeau, A review on wire-fed directed energy deposition based metal additive manufacturing, *J. Manuf. Mater. Process.* 7 (2023) 45, doi: 10.3390/jmmp7010045.
- [62] Z. Liu, D. Zhao, P. Wang, M. Yan, C. Yang, Z. Chen, J. Lu, Z. Lu, Additive manufacturing of metals: microstructure evolution and multistage control, *J. Mater. Sci. Technol.* 100 (2022) 224–236, <https://doi.org/10.1016/j.jmst.2021.06.011>.
- [63] A. Shrivastava, S. Anand Kumar, S. Rao, Postprocessing challenges in metal AM: Strategies for achieving homogeneous microstructure in Ni-based superalloys, in: *Advances in Metal Additive Manufacturing*, Elsevier, 2023, pp. 179–202, <https://doi.org/10.1016/B978-0-323-91230-3.00001-9>.
- [64] A.A.H. Hamers, C.M. Wayman, Shape memory behavior in FeMnCo alloys, *Scr. Metall. Mater.* 25 (1991) 2723–2728, [https://doi.org/10.1016/0956-716X\(91\)90146-R](https://doi.org/10.1016/0956-716X(91)90146-R).
- [65] Z. Xu, Martensitic transformation fcc(γ) \rightarrow hcp(ϵ), *Sci. China Ser. E: Technol. Sci.* 40 (1997) 561–566, <https://doi.org/10.1007/BF02916839>.
- [66] K. Yamauchi, I. Ohkata, K. Tsuchiya, S. Miyazaki, *Shape Memory and Superelastic Alloys Applications and Technologies*, 2011.
- [67] H. Yang, W. Yan, X. Deng, M. Zhang, Y. Wang, Improving the shape memory effect of a Fe-Mn-Si-Cr-Ni alloy through shot peening, *Materials* 15 (2022) 2585, <https://doi.org/10.3390/ma15072585>.
- [68] Q. Gu, J. van Humbeeck, L. Delaey, L. Federzoni, G. Guénin, D. Gex, Effect of amount of deformation on the martensitic transformation and shape memory effect in Fe-Mn-Si based shape memory steel, *Le J. Phys.que IV*. 05 (1995) C2-311–C2-315. doi: 10.1051/jp4:1995248.
- [69] C. Zhang, F. Song, S. Wang, H. Peng, Y. Wen, Effect mechanism of Mn contents on shape memory of Fe-Mn-Si-Cr-Ni alloys, *Acta Metall. Sin.* 51 (2015) 201–208.
- [70] J.P. Oliveira, Z. Zeng, T. Omori, N. Zhou, R.M. Miranda, F.M.B. Fernandes, Improvement of damping properties in laser processed superelastic Cu-Al-Mn shape memory alloys, *Mater. Des.* 98 (2016) 280–284, <https://doi.org/10.1016/j.matdes.2016.03.032>.
- [71] S. Li, D. Cong, Z. Chen, S. Li, C. Song, Y. Cao, Z. Nie, Y. Wang, A high-entropy high-temperature shape memory alloy with large and complete superelastic recovery, *Mater Res Lett.* 9 (2021) 263–269, <https://doi.org/10.1080/21663831.2021.1893233>.
- [72] G.Z. Voyiadjis, M. Yaghoobi, Introduction: size effects in materials, in: *Size Effects in Plasticity*, Elsevier, 2019, pp. 1–79, <https://doi.org/10.1016/B978-0-12-812236-5.00001-3>.